CMS Physics Analysis Summary

Contact: cms-pag-conveners-higgs@cern.ch 2019/09/30

A measurement of the Higgs boson mass in the diphoton decay channel

The CMS Collaboration

Abstract

A measurement of the mass of the Higgs boson in the diphoton decay channel is presented. This analysis is based on 35.9 fb^{-1} of proton-proton collision data collected in 2016 with the CMS detector at a center-of-mass energy of 13 TeV. The Higgs boson mass is measured to be $m_{\text{H}} = 125.78 \pm 0.26$ GeV. This is combined with a measurement of m_{H} already performed in the $\text{H} \to \text{ZZ}^* \to 4l$ decay channel using the same dataset, giving $m_{\text{H}} = 125.46 \pm 0.17$ GeV. This result, when combined with an earlier measurement of the Higgs boson mass using data collected in 2011 and 2012 with the CMS detector, gives a value for the Higgs boson mass of $m_{\text{H}} = 125.35 \pm 0.15$ GeV. In this note we summarize the strategy of this measurement in the $\text{H} \to \gamma\gamma$ final state emphasizing the methods employed to mitigate and to quantify the main sources of systematic uncertainty. The combination strategy is also described.

1 Introduction

The announcement in 2012 of independent observations of the Higgs boson (H) by the CMS and ATLAS Collaborations [1, 2] in proton-proton collisions at the CERN LHC was a key milestone in our understanding of the mechanism of electroweak symmetry breaking. More recently, with the higher luminosity available at the LHC between 2016 and 2018 (Run 2), our focus has shifted from observation to precision measurements of its properties. The couplings of this new particle with other elementary particles are predicted by the standard model (SM) of particle physics once its mass is known. This motivates precise measurements of the mass of the Higgs boson (m_{H}) in all available decay channels.

Although the $\mathrm{H} \to \gamma\gamma$ decay channel has a small ($\approx$0.23%) branching ratio, it provides a clean final state topology with a mass peak that can be reconstructed with high precision. The measurement of m_{H} in this decay channel can be combined with separate measurements in other decay channels to achieve a more precise measurement.

The mass of the Higgs boson was measured to be 125.09 ± 0.24 GeV [3], in a combined measurement performed with the data collected in 2011 and 2012 (Run 1) by the ATLAS and CMS Collaborations. More recently the ATLAS Collaboration has published a measurement of m_{H} of 124.97 ± 0.24 GeV [4] based on 36.1 fb^{-1} of Run 2 data combined with data from Run 1.

We present in this note a new measurement of m_{H} in the $\mathrm{H} \to \gamma\gamma$ decay channel with the 35.9 fb^{-1} of data collected at $\sqrt{s}$ = 13 TeV in 2016. The CMS Collaboration has previously reported a measurement of m_{H} with the same dataset in the $\mathrm{H} \to ZZ^* \to 4l$ decay channel where m_{H} was measured to be 125.26 ± 0.21 GeV [5]. The combined result and procedure followed for this combination is also described in this note.

2 The CMS detector

The central feature of the CMS detector is a superconducting solenoid of 6 m internal diameter with a uniform magnetic field of 3.8 T. Inside the magnet volume are a silicon pixel and strip trackers, a lead tungstate crystal electromagnetic calorimeter (ECAL), and a brass/scintillator hadron calorimeter, each composed of a barrel and two endcap sections. The ECAL is a hermetic homogeneous calorimeter made of 61,200 lead tungstate ($PbWO_4$) crystals mounted in the central barrel part, closed by 7,324 crystals in each of the two endcaps. In the region $1.65 < |\eta| < 2.6$ a three radiation length thick preshower detector with two orthogonal layers of silicon strips is placed in front of the endcap crystals. Avalanche photodiodes are used as photodetectors in the barrel and vacuum phototriodes in the endcaps. The barrel part of the ECAL (EB) covers the pseudorapidity range $|\eta| < 1.479$, while the endcap calorimeters cover the range $1.479 < |\eta| < 3.0$. A calorimeter with longitudinal quartz fibers complements the coverage provided by the barrel and endcap detectors. The first level of the CMS trigger system uses information from the calorimeters and muon detectors to select the most interesting events in a fixed time interval of less than 4 μs. The high-level trigger processor farm further decreases the event rate from around 100 kHz to around 1 kHz before data storage. A more detailed description of the CMS detector, together with a definition of the coordinate system and the relevant kinematic variables, can be found in Ref. [6].

3 Analysis strategy

The general strategy followed in this analysis is the same as that followed in an earlier analysis by the CMS Collaboration of the Higgs boson properties in the diphoton channel, published in Ref. [7]. Since that publication a more accurate detector calibration has become available. We have also improved the method, first introduced in Ref. [8], to measure and correct for non-linear discrepancies in the energy scale with transverse momentum (p_{T}) between data and simulation by increasing the granularity of the correction. In addition, we have developed a method to evaluate the systematic uncertainty of the photon energy scale due to radiation damage of the ECAL crystals, and we have simplified the event categorisation in the analysis.

With the new calibration, the detector response is more stable with time, leading to a reduction of the uncertainties in the corrections to the photon energy due to the material upstream of the ECAL and for the shower containment.

These improvements were made to improve the precision of the measurement of m_{H} through a better understanding of the systematic uncertainties of the measurement.

4 Data and simulation

In the data collection events were selected with a diphoton trigger that had asymmetric p_T thresholds of 30 and 18 GeV. Full details of the trigger selection and the measurement of the trigger efficiency can be found in Ref. [7].

The signal sample is simulated with the MADGRAPH5_aMC@NLO v2.2.2 matrix-element generator [9] at next-to-leading order and interfaced with PYTHIA 8.205 [10], for parton showering and hadronization. The PYTHIA underlying event tune CUETP8M1 [11] was used.

The irreducible prompt diphoton background and the reducible backgrounds of γ+jets and multijet events, where the jets are misidentified as isolated photons, are the dominant backgrounds to the $\mathrm{H} \to \gamma\gamma$ decay process. The diphoton background is modelled with the SHERPA v.2.2.1 [12] generator, which includes the Born processes with up to 3 additional jets at leading-order (LO) accuracy, as well as the LO box processes. The γ+jets and multijet backgrounds are modelled with PYTHIA at LO. A filter is applied for the production of these samples to enhance the production efficiency by preferentially selecting jets with a relatively large fraction of electromagnetic energy. These samples are used for the training of the multivariate discriminants used in this analysis, as well as for the optimisation of the event categorisation. Drell-Yan samples, used to derive the electron and photon energy scale corrections and their systematic uncertainties, are simulated with MADGRAPH [13] and MADGRAPH5_aMC@NLO.

All simulated events are propagated through the full CMS detector simulation using the GEANT4 package [14].

The simulations include multiple proton-proton interactions taking place within a bunch crossing, known as 'pileup'. Pileup can occur not only in the same bunch crossing (in-time pileup), but in the crossing of previous and subsequent bunches (out-of-time pileup). The simulated events are scaled to reproduce the distribution of in-time pileup in data.

5 Photon reconstruction and identification

Photon candidates are reconstructed as energy deposits in a collection of crystals in the ECAL. A cluster is formed by first identifying a 'seed' crystal with an energy above a given threshold,

then the cluster is built by finding the crystals that share an edge with the seed crystal and have an energy above another lower threshold. This second threshold is set to be approximately 80 MeV in the barrel and ranging from 80 to 300 MeV in the endcaps, depending on $|\eta|$. These clusters, once formed, are combined to form a 'supercluster', which contains the shower of the photon. This procedure accounts for variations in geometry as a function of $|\eta|$, and optimises the robustness of the energy resolution against pileup.

5.1 Photon energy calibration

A critical component of the measurement of m_{H} is the energy calibration of the response of the ECAL to photons. The energy of a photon is calculated by summing the calibrated and corrected energy [15] of all crystals in the associated supercluster, and the energy deposited in the preshower in the region $1.65 < |\eta| < 2.6$ covered by this detector. For each supercluster a shower shape variable R_9 is defined, which is used to select photons undergoing a conversion in the material between the interaction point and the front face of the ECAL. The variable R_9 is defined for a candidate electromagnetic cluster as the ratio of the sum of energy deposited in a 3×3 crystal array, centred on the crystal with the highest energy, to the sum of the energy in the whole cluster. The energy deposition of photons that interact before reaching the calorimeter tends to have wider transverse profiles and thus lower values of R_9 than those of unconverted photons. To further optimize the energy resolution, the energy is corrected for the lack of complete containment of the electromagnetic showers in the clustered crystals, the energy lost by photons that convert upstream of the calorimeter, and the effects of pileup. These corrections are derived using a multivariate regression technique, trained on simulated events, which simultaneously estimates the energy of the photon and its median uncertainty. The inputs to this regression are shower shape variables, the preshower information, and observables sensitive to pileup [16].

After applying these corrections to the photon energy, some residual differences remain between the data and simulation in both the photon energy scale and the resolution. A multistep procedure is used to correct for these differences so that the simulation accurately reproduces the data. In the first step of this process, any residual long-term drifts in the energy scale in data are corrected for, in approximately 18-hour intervals corresponding to one LHC fill, using $\mathrm{Z} \to \mathrm{ee}$ decays. In the second step, corrections to both the energy resolution in the simulation, and the scale correction needed for the data are derived simultaneously in bins of $|\eta|$ and R_9 for electrons. The energy resolution obtained in simulation is matched to the data by adding a Gaussian smearing term, determined by adjusting the agreement in the $\mathrm{Z} \to \mathrm{ee}$ invariant mass distributions. Then in the third and final step the energy scale corrections are derived in bins of $|\eta|$ and p_{T} to account for any non-linear response of the crystals with energy. The corrections obtained from this step are shown in Fig. 1 for electrons in the three bins of $|\eta|$ in the ECAL barrel region. This additional step in the scale correction improves the precision of the Higgs boson mass measurement, since the energy spectrum of the electrons from Z boson decay ($\langle p_{\mathrm{T}} \rangle \approx 45\,\mathrm{GeV}$) used to derive the scale corrections, is different from the energy spectrum of photons from Higgs boson decay ($\langle p_{\mathrm{T}} \rangle \approx 60\,\mathrm{GeV}$).

We note that in the second step the binning in R_9 for the scale corrections has been increased by a factor of five over the previous analysis [7], resulting in an improvement in the precision with which the energy scale is derived. Also, as a consistency test after the correction factors are derived in the second and the third steps, they are applied to the data and a new set of factors are derived. Any deviation from unity is an indication of the non-closure of the process and is applied as a systematic uncertainty.

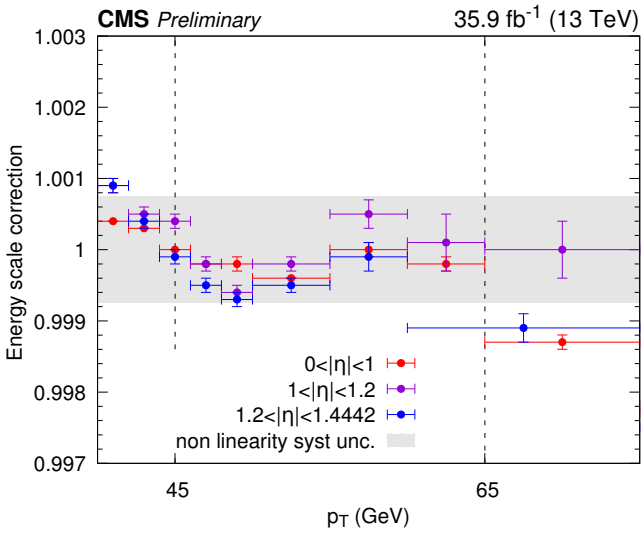

Figure 1: Energy scale corrections applied to data as function of the p_T of the photon. The systematic uncertainty associated to this correction is approximately the maximum deviation observed in the p_T range between 45 and 65 GeV for electrons in the ECAL barrel region.

The agreement between data and simulation in the dielectron invariant mass, after applying these energy scale corrections and the additional smearings, is shown in Fig. 2 for dielectron events in the barrel with R_9 greater than 0.94, and for dielectron events with a leading transverse energy between 55 and 65 GeV, without a requirement on the second electron. The former demonstrates the performance of the energy corrections on photons with the highest statistics, optimal resolution, and the highest sensitivity to the Higgs boson mass. The latter demonstrates that the energy corrections are effective in a kinematic region where the p_{T} of the electron has been chosen to be the typical p_{T} of a photon from a Higgs boson decay. In both cases we observe an excellent agreement between data and simulation in the core of the distributions.

5.2 Photon preselection and identification

The photons considered in the subsequent steps of this analysis are required to satisfy certain preselection criteria that are similar to but more stringent than those imposed by the trigger requirements. A detailed description of these preselection criteria as well the methods employed to evaluate their efficiencies can be found in Ref. [7]. A dedicated boosted decision tree (BDT) is used to classify prompt photons from other photon candidates that arise out of misidentified jet fragments, but which satisfy the preselection criteria. The full details of the input features of this photon identification BDT is also described in Ref. [7]. The score of this BDT is used later in the event categorization, discussed in the subsequent section.

5.3 Vertex Selection

The choice of the diphoton vertex position along the beam axis has a direct impact on the diphoton mass resolution, since if the vertex position is known to better than about 1 cm, then the invariant mass resolution is dominated by the photon energy resolution. The distribution of the position of the interaction vertices along the beam axis has an RMS spread of about 3.4 cm, and, in typical pileup conditions in 2016, there were on average around 23 interactions in each bunch crossing. The choice of the diphoton vertex is made following the same procedure in Ref. [7]: a BDT, whose inputs are observables related to tracks recoiling against the diphoton

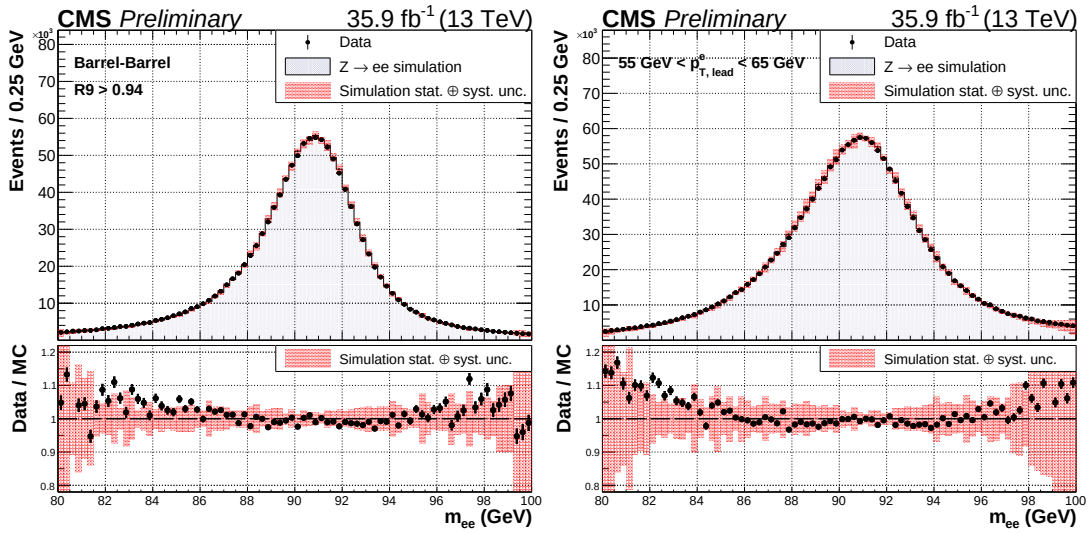

Figure 2: Comparison of the distributions of the invariant mass of the dielectrons in data and simulation in $Z \to ee$ events after application of energy corrections in two representative categories. Left: Both electrons are in the ECAL barrel and satisfy $R_9 > 0.94$. Right: The leading electron has a transverse momentum between 55 and 65 GeV, without a requirement on the second electron. The systematic uncertainty in the error band in the plots include only the uncertainties on the derived energy scale corrections.

system is used to identify the most likely vertex, and a second BDT is used to determine the probability of correctly choosing that vertex. The score of the second BDT is used later in the event categorisation, discussed below. The algorithm is validated using $Z \to \mu^+\mu^-$ events with the muon tracks removed so as to mimic diphoton pair production. The efficiency of assigning the event to a vertex within 1 cm of the true vertex in the simulated $H \to \gamma\gamma$ events is found to be approximately 81%.

6 Event Classification

The event selection procedure is similar to that in Ref. [7]. The p_T of the two leading photons ($p_T^{\gamma 1}$, $p_T^{\gamma 2}$) are required to satisfy $p_T^{\gamma 1} > m_{\gamma\gamma}/3$ and $p_T^{\gamma 2} > m_{\gamma\gamma}/4$, where the photon p_T requirement is applied after the vertex assignment. Additionally $m_{\gamma\gamma}$ is required to be between 100 and 180 GeV. The use of $m_{\gamma\gamma}$ scaled p_T thresholds is to prevent a distortion of the lower end of the invariant mass spectrum. The superclusters of both photons are required to have a pseudo-rapidity $|\eta| < 2.5$ and to be outside of the barrel-endcap transition region, $1.44 < |\eta| < 1.57$.

To improve the sensitivity of the analysis, events are classified according to their production mechanism, mass resolution, and their predicted signal-to-background ratio. A dedicated classifier referred to as the diphoton BDT is used to discriminate between signal and background events. This BDT assigns a high score to events with photons showing signal-like kinematics, a good mass resolution, and a high score from the photon identification BDT. The per-event probability estimate of assigning the correct primary vertex to the diphoton is used as one of the input features of this diphoton BDT. The other input features are described in Ref. [7].

Nearly 95% of Higgs boson events come from two production modes. These are gluon-gluon

fusion (ggH) and vector-boson fusion (VBF), where there are two jets in the final state separated by a large rapidity gap. A multivariate discriminant is trained to discriminate VBF events from ggH + jets events, using the kinematics of the characteristic VBF dijet system as inputs. This discriminant is then given as an input to an additional multivariate classifier (VBF combined BDT) along with the score from the diphoton BDT, and the ratio $p_{\mathrm{T}}^{\gamma\gamma}/m_{\gamma\gamma}$. The VBF events are subdivided into three categories based on the VBF combined BDT score. The remaining events are mostly ggH events and are designated as 'untagged'. These events are further subdivided into four categories based on their diphoton BDT score.

Adding other possible analysis categories, where for example, the Higgs boson is produced in association with a vector boson, or with a pair of top quarks, adds only a small increment to the precision of the mass measurement at the cost of a significant increase in the analysis complexity. Thus these production modes are not considered as separate categories in the analysis.

Other event categorisation schemes specifically defined for the measurement of m_{H} were investigated, but did not show any improvement over the event categorisation scheme described in Ref [7], and were not used in this analysis.

7 Signal and background models

In order to extract the mass of the Higgs boson, signal and background models are constructed to fit the diphoton mass distributions observed in the data. Since the resolution of the Higgs boson mass in the diphoton channel depends on the production mechanism and analysis category, a signal model is derived for each category using simulated Higgs boson events. The background model used in the fit of the diphoton mass spectrum is derived directly from the data.

7.1 Signal model

The signal shapes for the diphoton invariant mass distributions are derived for every analysis category and with a nominal Higgs boson mass m_{H}, using simulated events from the different production modes. The simulation accounts for the trigger, reconstruction and identification efficiencies, which are measured with data-driven techniques. A weighting is applied to the simulated events so that the distribution of the number of interactions and the location of the primary vertex is matched to the distributions observed in data. A detailed description of each of these steps can be found in Ref. [7].

Since the distribution of $m_{\gamma\gamma}$ depends on the correct assignment of the vertex associated with the diphoton candidate, signal models were constructed with correct and wrong vertex assignment scenarios separately. For each process, analysis category, and vertex scenario, the $m_{\gamma\gamma}$ distributions were fit with a sum of, at most, five Gaussian functions.

For each process, analysis category, and vertex scenario, a simultaneous fit of the signal samples at mass values ranging from 120 to 130 GeV is performed to obtain the variations of the Gaussian function parameters, described by polynomials in m_{H}, used in the signal model fit.

The final fit function for each category is obtained by summing the functions for all production modes normalised to the expected signal yields in that category. Fig. 3 shows the signal model corresponding to $m_{\mathrm{H}} = 125$ GeV for the best resolution category, which is the untagged events with the highest diphoton BDT score, 'Untagged 0'. Also shown in the same figure is the signal model for the sum of all categories, with each category weighted by the corresponding S/(S+B)

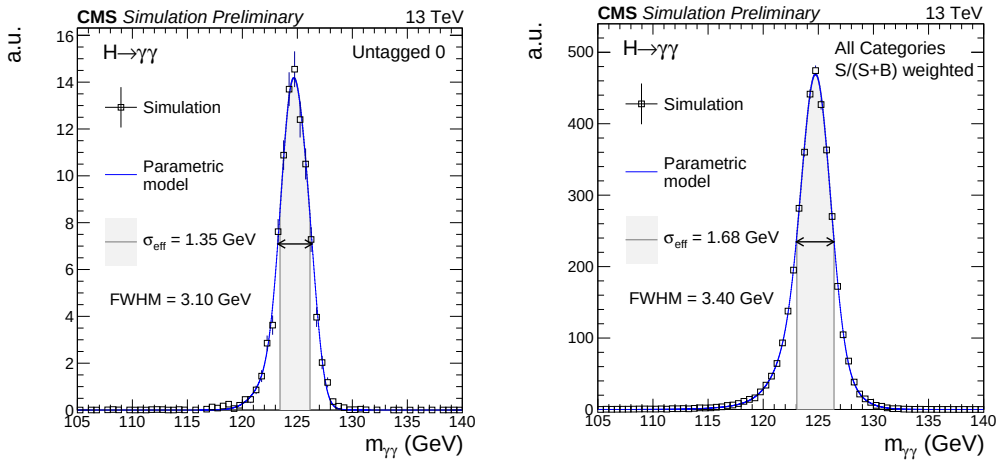

Figure 3: The signal shape models for the highest resolution analysis category (left), and the sum of all categories combined together after scaling each of them by the corresponding S/(S+B) ratio (right) for a simulated H $\rightarrow \gamma\gamma$ signal sample with $m_{\mathrm{H}} = 125$ GeV. The open squares represent weighted simulation events and the blue line the corresponding model. Also shown is the σ_{eff} value (half the width of the narrowest interval containing 68.3% of the invariant mass distribution) and the full width at half of the maximum (FWHM).

ratio, where S is the number of signal events, and B is the number of background events in a window around the m_{H} peak. In the figure the effective width (σ_{eff}), defined as half of the smallest interval that contains 68.3% of the invariant mass distribution, is given, as is the full width at half maximum (FWHM).

7.2 Background model

The model used to describe the background for each of the analysis categories is obtained from data using the discrete profiling method, which is described in Ref. [17]. In this method a large set of candidate function families are considered, including exponential functions, Bernstein polynomials, Laurent series, and power law functions. These are fit to the $m_{\gamma\gamma}$ distribution in the mass range of 100 to 180 GeV. For each family of functions, an F-test [18] is performed to determine the maximum order to be used in the fit, while the minimum order is determined by placing a requirement on the goodness of the fit to the data. The choice of the background function is treated as a discrete nuisance parameter in the fit to account for the uncertainty associated with the arbitrary choice of the function.

8 Systematic uncertainties

The systematic uncertainties are treated differently depending on their effect on the diphoton invariant mass distributions in the different signal categories. The systematic uncertainties on the photon energy scale and resolution modify the shape of the diphoton mass distribution in the signal model. Other systematic uncertainties, while not affecting the signal shape, affect the event yield.

The sources of uncertainty included in all CMS H $\rightarrow \gamma\gamma$ analyses are described in Ref. [7]. However, for this analysis a more precise determination of the systematic uncertainties in the

photon energy scale is required and is described here.

8.1 Uncertainties on the photon energy scale estimated with electrons

The following sources of systematic uncertainties on the photon energy scale were first estimated from electrons and directly propagated to the photons.

- *Electron energy scale and resolution*: the uncertainty on the electron energy scale and resolution corrections are derived using $Z \to ee$ events by varying the distribution of R_9, varying the electron selection cuts used in the derivation of the corrections, varying the transverse energy thresholds on the electron pairs used in the derivation of the corrections and the non-closure of the method used to derive the electron scale corrections. This uncertainty is 0.05–0.1% for electrons in the barrel of the ECAL, and 0.1–0.3% for electrons in the endcap of the ECAL.
- *Residual p_T dependence of the energy scale correction*: Since the corrections for the residual differences between data and MC were estimated with $Z \to ee$ events ($\langle p_T \rangle \approx 45\,\text{GeV}$), applying them to photons with $\langle p_T \rangle \approx 60\,\text{GeV}$ introduces an additional systematic error. The non-closure of the p_T dependent electron energy scale corrections, as described in Section 5.1, is used as the estimate of this source of uncertainty. For electrons having a $p_T < 80\,\text{GeV}$ this uncertainty is 0.075%, while for electrons having transverse energy greater than 80 GeV the uncertainty is 0.15%. This uncertainty is applied conservatively on the global energy scale, correlated among all photons.

8.2 Uncertainties due to differences between electrons and photons

Additional systematic uncertainties due to the differences between the response of ECAL to electrons and photons were studied and assigned as follows:

- *Modelling of the material budget*: The uncertainty in the material budget between the interaction point and the ECAL, which affects electron and photon showers differently, was evaluated as described in Ref. [7] and is at most 0.24% of the photon energy scale.
- *Non-uniformity of the light collection*: Since the shower maximum for photons is deeper than that of electrons by approximately one radiation length (0.89 cm in lead tungstate), differences in the light collection efficiency (LCE) along the length of the crystals will introduce a difference in the ECAL response to electrons and photons. To account for this an additional systematic uncertainty is assigned to the photon energy scale. Due to the increase in the radiation damage to the ECAL crystals in Run 2 compared to Run 1, the impact of the non-uniformity in light collection has become more important. Therefore a special effort has been made to study this effect and to better estimate the associated systematic uncertainty on the photon energy scale. This is estimated using the LCE model described in Ref. [19]. It is derived from an optical simulation [20] and qualified with measurements made with irradiated crystals. This model takes into account the non-uniformity of the collection of scintillation light due to radiation damage and the crystal geometry. This uncertainty has been evaluated as a function of transverse momentum, supercluster $|\eta_{SC}|$, and R_9 using the radiation damage conditions experienced in 2016. The results are summarised in Fig. 4. The effect is less than 0.16% in the barrel and less than 0.45% in the endcap, and affects photons with $R_9 > 0.96$ the most. The uncertainty is assumed to be correlated among the different $|\eta|$ and R_9 bins but uncorrelated between the barrel and the endcap regions due to the difference in the degree of radiation damage, crystal

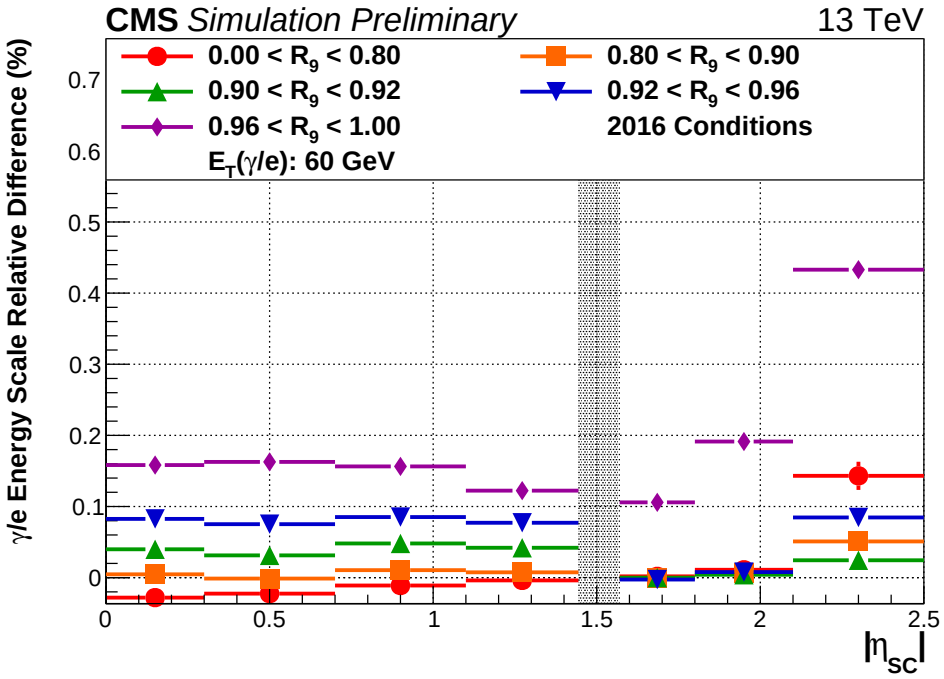

Figure 4: The systematic uncertainty due to the difference between the electron and photon energy scale due to radiation damage induced non-uniformity of light collection in ECAL crystals in different supercluster $|\eta_{SC}|$ and R_9 categories. The method used to evaluate this is described in Section 8.2.

size and surface treatment.

- *Mis-modelling of the input variables to the energy correction*: The uncertainty on the photon energy scale due to imperfect modelling of the shower shape in the simulation is found to be negligible (less than 10 MeV). The reason it is negligible is because of the good agreement between the data and simulation of the different input variables used in the the photon energy regression correction, resulting from the updated detector calibration described in Section 3.

8.3 Impact of the sources of uncertainty

The contribution of each source of the photon energy scale systematic uncertainty to the total uncertainty on the m_{H} measurement was evaluated by performing a likelihood scan removing all but that source and subtracting the statistical uncertainty in quadrature. The results are summarised in Table 1. It can be seen that the leading sources of systematic uncertainty affecting m_{H} are the residual p_T dependence of the photon energy scale, non-uniformity of light collection and the electron energy scale and resolution correction.

9 Results

To extract the measured value of m_{H} and its uncertainty, a binned maximum likelihood fit is performed simultaneously to the $m_{\gamma\gamma}$ distributions of all analysis categories, in the range $100 < m_{\gamma\gamma} < 180$ GeV. We use binned fits to reduce computation time and a bin size of 125 MeV,

Table 1: The observed impact of the different sources of systematic uncertainty on the measurement of m_{H}

Source	Contribution [GeV]
Electron energy scale and resolution corrections	0.10
Residual p_T dependence of the photon energy scale	0.11
Modelling of the material budget	0.03
Non-uniformity of the light collection	0.11
Statistical uncertainty	0.18
Total uncertainty	0.26

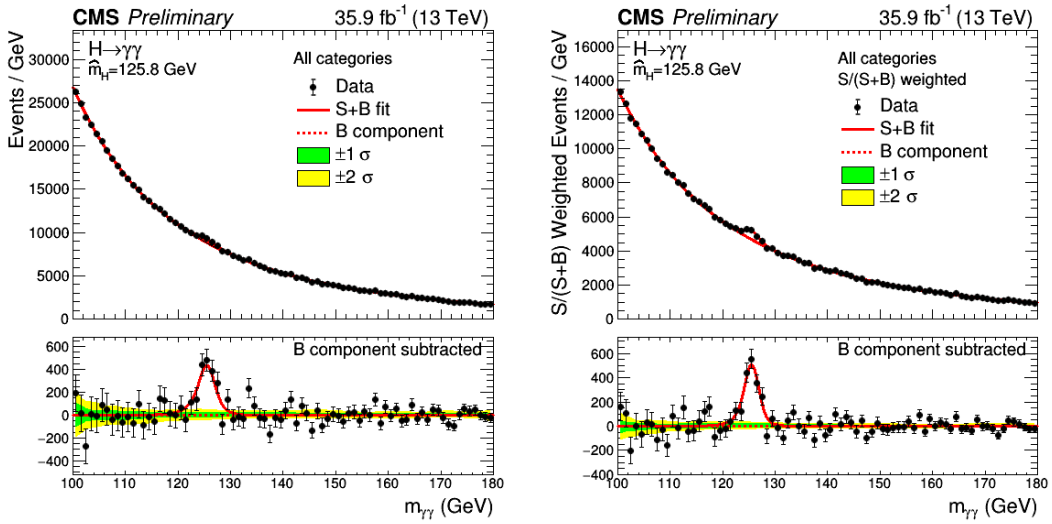

Figure 5: Data and signal-plus-background model fits for all categories summed (left) and where the categories are summed weighted by their sensitivity (right). The one (green) and two (yellow) standard deviation bands include the uncertainties in the background component of the fit. The lower panel in each plot shows the residuals after the background subtraction.

which is small compared to the mass resolution. The data and the signal-plus-background model fit for the sum of all analysis categories is shown in Fig. 5.

The expected number of signal events for each category is summarised in Fig. 6, where the contribution of each production mode to each analysis category is shown. The σ_{eff} and σ_{HM} are also listed: the latter is the FWHM, divided by 2.35.

In the likelihood scan of the Higgs boson mass, other parameters of the signal and background models are allowed to vary. Systematic uncertainties are included in the form of nuisance parameters, and the results are obtained using an asymptotic approach [21, 22] with a test statistic based on the profile likelihood ratio [23]. In the fit to extract m_{H} two independent signal strengths $\mu_{\mathrm{ggH+ttH}}$ and $\mu_{\mathrm{VBF+VH}}$ are free to vary. The best-fit mass of the Higgs boson is observed to be $m_{\mathrm{H}} = 125.78 \pm 0.18$ (stat) ± 0.18 (syst) GeV, while it was expected to have a statistical uncertainty of ± 0.21 GeV and a systematic uncertainty of ± 0.18 GeV. The expected uncertainties on the measurement were obtained by generating an Asimov data set [23] from the expected signal from SM plus best-fit background model.

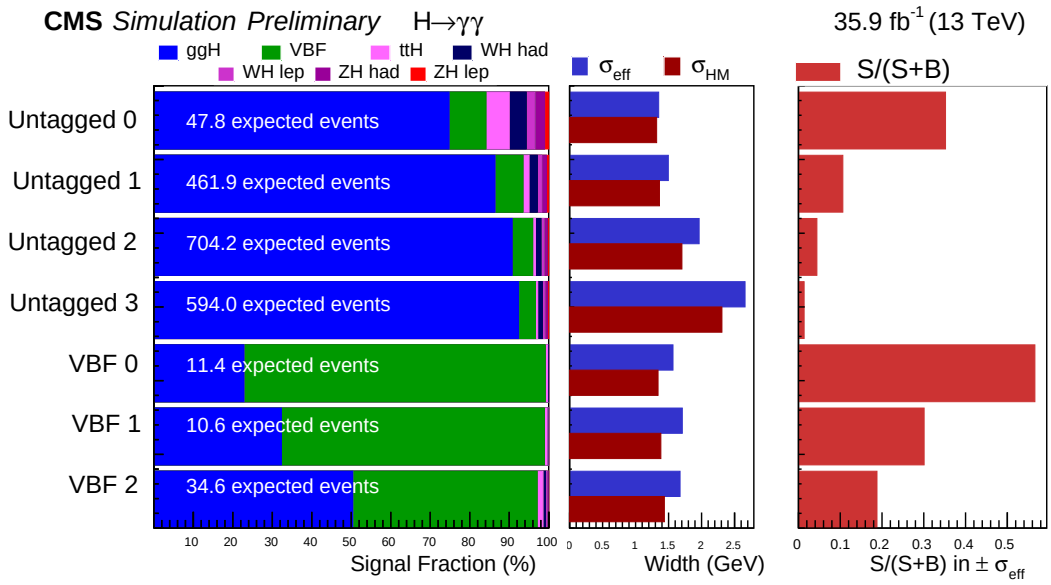

Figure 6: The expected number of signal events per category and the percentage breakdown per production mode. The σ_{eff} value (half the width of the narrowest interval containing 68.3% of the invariant mass distribution) is also shown as an estimate of the $m_{\gamma\gamma}$ resolution in that category and compared directly to the σ_{HM}. The ratio of the number of signal events (S) to the number of signal plus background events (S+B) is shown on the right hand side.

9.1 Combination with the H $\rightarrow ZZ^* \rightarrow 4l$ mass measurement with the 2016 data set

The results of this mass measurement were combined with a measurement of the same quantity in the H $\rightarrow ZZ^* \rightarrow 4l$ decay channel with the 2016 data set reported by CMS in Ref. [5] using the same data set with a preliminary set of detector conditions.

In the combination the uncertainty associated to the luminosity measurement was taken to be fully correlated between both decay channels. The only other uncertainty that could be correlated across the two decay channels is the uncertainty in the electron and photon energy scale. To investigate the maximum impact of a correlation we used pseudo-experiments to show that even if the energy scales were fully correlated between the two decay channels, treating them as uncorrelated does not bias the best-fit m_{H} value. We therefore treat this source of uncertainty to be uncorrelated between the two decay channels. From a further study based on pseudo-experiments we concluded that if the energy scales were fully correlated between the two decay channels, treating them as uncorrelated leads to an underestimation of the total uncertainty on m_{H} by approximately 5%. We account for this by increasing the total uncertainty by 5% when the measurements of m_{H} in the H $\rightarrow \gamma\gamma$ and the H $\rightarrow ZZ^* \rightarrow 4l$ decay channels using the 2016 dataset are combined.

The combined value of the Higgs boson mass measured from the 2016 data set is observed to be $m_{\text{H}} = 125.46 \pm 0.13\,(\text{stat}) \pm 0.11\,(\text{syst})$ GeV with an expected statistical uncertainty of $\pm$ 0.16 GeV and a systematic uncertainty of $\pm$ 0.11 GeV. As before, the two common signal strengths $\mu_{\text{ggH+ttH}}$ and $\mu_{\text{VBF+VH}}$ are free to vary in the fit to extract the Higgs boson mass. This result is in good agreement with the ATLAS+CMS Run 1 measurement [3], $m_{\text{H}} = 125.09 \pm 0.24$ GeV. A scan of the value of twice the negative logarithm of the likelihood (-2ΔNLL) as a function of m_{H}

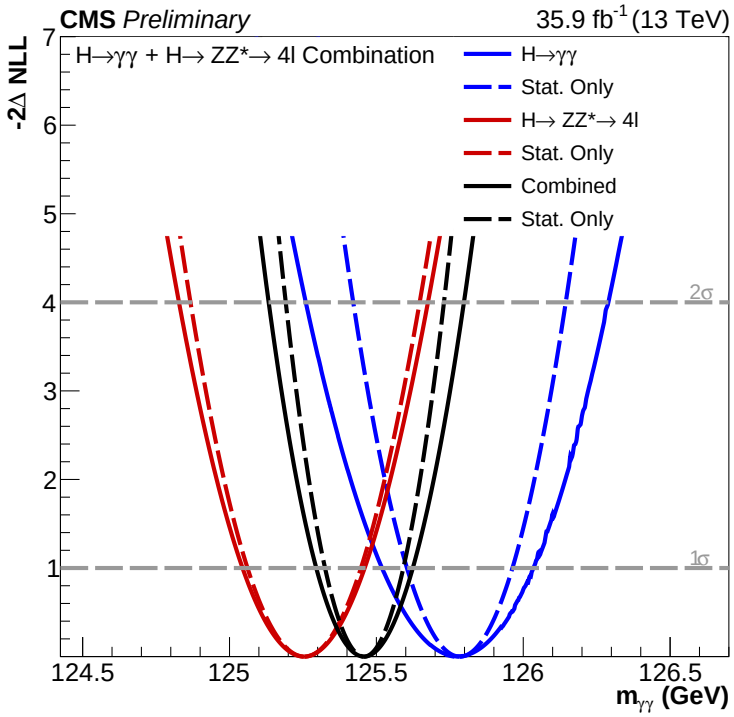

Figure 7: The likelihood scan of the measured Higgs boson mass in the H $\rightarrow \gamma\gamma$ and H $\rightarrow ZZ^* \rightarrow 4l$ decay channels individually and for the combination with the 2016 data set. The solid lines are for the full likelihood scan including all systematic uncertainties, while the dashed lines denote the same with the statistical uncertainty only. The additional 5% uncertainty due to treating the electron and photon energy scales as uncorrelated between the two decay channels for the combination is not included in the combined likelihood scan.

for the two individual decay channels, as well as their combination is shown in Fig. 7. The same procedure was used to combine this result from the 2016 data set with the same measurement (H $\rightarrow \gamma\gamma$ and H $\rightarrow ZZ^* \rightarrow 4l$) obtained from the Run 1 data [24]. The total uncertainty on m_{H} obtained by combining the two decay channels for Run 1 and the 2016 data sets is also increased by 5% for the same reason described earlier in the context of the combination with the 2016 data set alone. For the combined measurement performed in Run 1 [24] there was no additional uncertainty included due to the uncorrelated treatment of the electron and photon energy scales in the two decay channels. The result of combining the measurements from both data taking periods is $m_{\mathrm{H}} = 125.35 \pm 0.12\,(\mathrm{stat}) \pm 0.09\,(\mathrm{syst})$ GeV. Fig. 8 shows the likelihood scans of the combined Higgs boson mass in the H $\rightarrow \gamma\gamma$ and H $\rightarrow ZZ^* \rightarrow 4l$ decay channels with the Run 1 and 2016 data sets individually and the same combining the two data sets. A summary of the individual and combined measurements in Run 1 and 2016 is shown in Fig. 9.

10 Summary

In this note we have described a measurement of the Higgs boson mass in the diphoton decay channel. This analysis has taken advantage of the higher integrated luminosity data collected in 2016 at $\sqrt{s} = 13\,\mathrm{TeV}$ at the CERN LHC. New analysis techniques have been introduced to improve the precision of the measurement and we have used an improved detector calibration. The techniques that are new with respect to the previous analysis in the diphoton decay channel [7] are the introduction of residual energy corrections in much finer bins of the

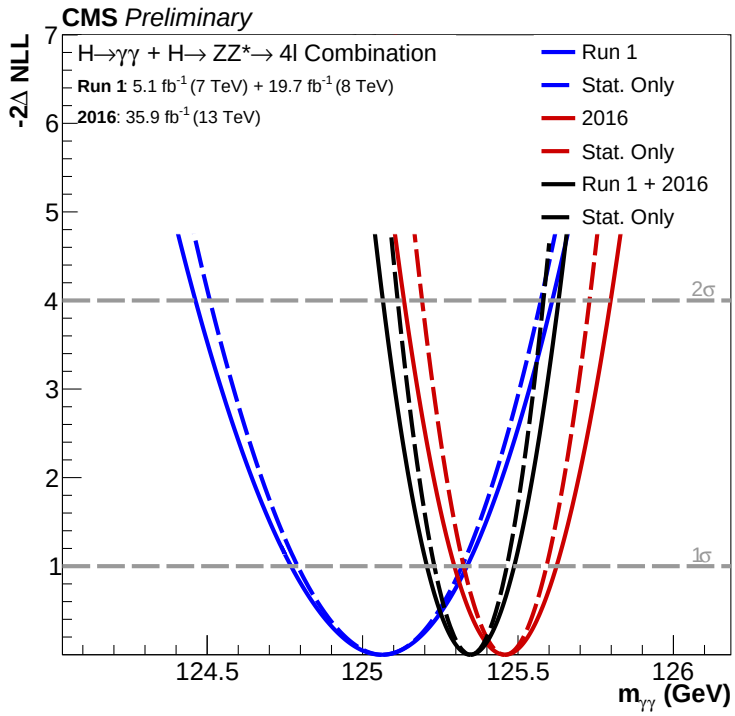

Figure 8: The likelihood scan of the combined Higgs boson mass in the H $\rightarrow \gamma\gamma$ and H $\rightarrow ZZ^* \rightarrow 4l$ decay channels with the Run 1 and 2016 data sets individually and the same combining the two data sets. The solid lines are for the full likelihood scan including all systematic uncertainties, while the dashed lines denote the same with the statistical uncertainty only. The additional 5% uncertainty due to treating the electron and photon energy scales as uncorrelated between the two decay channels for the combination with the 2016 data set and the Run 1 + 2016 data sets is not included in the corresponding combined likelihood scans.

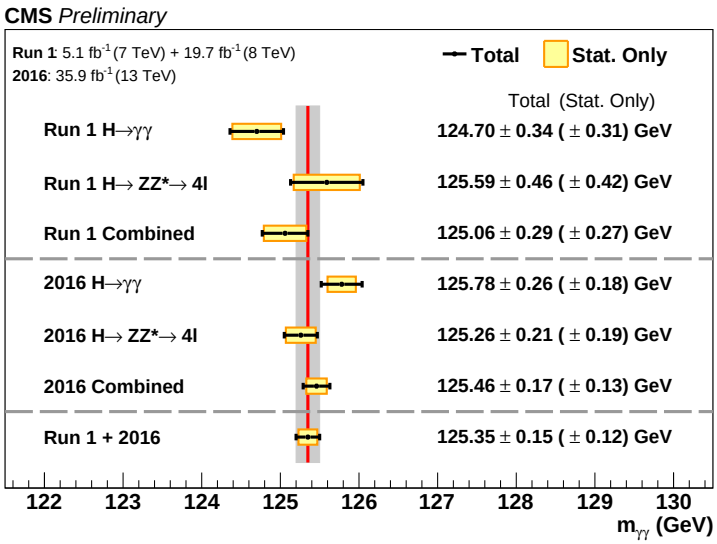

Figure 9: A summary of the measured Higgs boson mass individually in the H $\rightarrow \gamma\gamma$ and H $\rightarrow ZZ^* \rightarrow 4l$ decay channels, and for the combination of the two is presented here. The statistical (wider, yellow-shaded bands), and total (black error bars) uncertainties are indicated. The (red) vertical line and corresponding (gray) shaded column indicate the central value and the total uncertainty of the Run 1 + 2016 combined measurement, respectively.

shower-shape variable, R_9, and η, and the development of a procedure to derive p_T dependent corrections to the photon energy scale. We have also employed a new method to estimate the systematic uncertainty due to changes in the transparency of the ECAL crystals with radiation damage. The measured value of the Higgs boson mass in the diphoton decay channel is found to be $m_H = 125.78 \pm 0.26$ GeV. This measurement has been combined with a recent measurement by CMS of the same quantity in the H $\rightarrow ZZ^* \rightarrow 4l$ decay channel [5] to obtain a value of $m_H = 125.46 \pm 0.17$ GeV. Furthermore, when the Run 2 result with the 2016 data set is combined with the same measurement performed in Run 1 at 7 and 8 TeV the value of the Higgs boson mass is found to be $m_H = 125.35 \pm 0.15$ GeV.

References

[1] CMS Collaboration, "Observation of a new boson at a mass of 125 GeV with the CMS experiment at the LHC", *Phys. Lett. B* **716** (2012) 30, doi:10.1016/j.physletb.2012.08.021, arXiv:1207.7235.

[2] ATLAS Collaboration, "Observation of a new particle in the search for the Standard Model Higgs boson with the ATLAS detector at the LHC", *Phys. Lett. B* **716** (2012) 1, doi:10.1016/j.physletb.2012.08.020, arXiv:1207.7214.

[3] ATLAS, CMS Collaboration, "Combined Measurement of the Higgs Boson Mass in pp Collisions at $\sqrt{s} = 7$ and 8 TeV with the ATLAS and CMS Experiments", *Phys. Rev. Lett.* **114** (2015) 191803, doi:10.1103/PhysRevLett.114.191803, arXiv:1503.07589.

[4] ATLAS Collaboration, "Measurement of the Higgs boson mass in the $H \to ZZ^* \to 4\ell$ and $H \to \gamma\gamma$ channels with $\sqrt{s} = 13$ TeV pp collisions using the ATLAS detector", *Phys. Lett. B* **784** (2018) 345, doi:10.1016/j.physletb.2018.07.050, arXiv:1806.00242.

[5] CMS Collaboration, "Measurements of properties of the Higgs boson decaying into the four-lepton final state in pp collisions at $\sqrt{s} = 13$ TeV", *JHEP* **11** (2017) 047, doi:10.1007/JHEP11(2017)047, arXiv:1706.09936.

[6] CMS Collaboration, "The CMS experiment at the CERN LHC", *JINST* **3** (2008) S08004, doi:10.1088/1748-0221/3/08/S08004.

[7] CMS Collaboration, "Measurements of Higgs boson properties in the diphoton decay channel in proton-proton collisions at $\sqrt{s} = 13$ TeV", *JHEP* **11** (2018) 185, doi:10.1007/JHEP11(2018)185, arXiv:1804.02716.

[8] CMS Collaboration, "Observation of the diphoton decay of the Higgs boson and measurement of its properties", *Eur. Phys. J. C* **74** (2014) 3076, doi:10.1140/epjc/s10052-014-3076-z, arXiv:1407.0558.

[9] J. Alwall et al., "The automated computation of tree-level and next-to-leading order differential cross sections, and their matching to parton shower simulations", *JHEP* **07** (2014) 079, doi:10.1007/JHEP07(2014)079, arXiv:1405.0301.

[10] T. Sjstrand, S. Mrenna, and P. Skands, "A Brief Introduction to PYTHIA 8.1", *Comput. Phys. Commun.* **178** (2007) 852, doi:10.1016/j.cpc.2008.01.036, arXiv:0710.3820.

[11] CMS Collaboration, "Event generator tunes obtained from underlying event and multiparton scattering measurements", *Eur. Phys. J. C* **76** (2016) 155, doi:10.1140/epjc/s10052-016-3988-x, arXiv:1512.00815.

[12] T. Gleisberg et al., "Event generation with SHERPA 1.1", *JHEP* **02** (2009) 007, doi:10.1088/1126-6708/2009/02/007, arXiv:0811.4622.

[13] J. Alwall et al., "MadGraph 5 : Going Beyond", *JHEP* **06** (2011) 128, doi:10.1007/JHEP06(2011)128, arXiv:1106.0522.

[14] GEANT4 Collaboration, "GEANT4—a simulation toolkit", *Nucl. Instrum. Meth. A* **506** (2003) 250, doi:10.1016/S0168-9002(03)01368-8.

[15] CMS Collaboration, "Energy Calibration and Resolution of the CMS Electromagnetic Calorimeter in pp Collisions at $\sqrt{s} = 7$ TeV", *JINST* **8** (2013) P09009, doi:10.1088/1748-0221/8/09/P09009, arXiv:1306.2016. [JINST8,9009(2013)].

[16] CMS Collaboration, "Performance of Photon Reconstruction and Identification with the CMS Detector in Proton-Proton Collisions at sqrt(s) = 8 TeV", *JINST* **10** (2015) P08010, doi:10.1088/1748-0221/10/08/P08010, arXiv:1502.02702.

[17] P. D. Dauncey, M. Kenzie, N. Wardle, and G. J. Davies, "Handling uncertainties in background shapes: the discrete profiling method", *JINST* **10** (2015) P04015, doi:10.1088/1748-0221/10/04/P04015, arXiv:1408.6865.

[18] R. A. Fisher, "On the interpretation of χ^2 from contingency tables, and the calculation of P", *Journal of the Royal Statistical Society* **85** (1922) 87.

[19] T. Adams et al., "Beam test evaluation of electromagnetic calorimeter modules made from proton-damaged $PbWO_4$ crystals", *Journal of Instrumentation* **11** P04012, doi:10.1088/1748-0221/11/04/p04012.

[20] F. Gentit, "Litrani: a general purpose monte-carlo program simulating light propagation in isotropic or anisotropic media", *Nucl. Inst. Meth. A* **486** (2002) 35.

[21] T. Junk, "Confidence level computation for combining searches with small statistics", *Nucl. Instrum. Meth. A* **434** (1999) 435, doi:10.1016/S0168-9002(99)00498-2, arXiv:hep-ex/9902006.

[22] A. L. Read, "Presentation of search results: the CLs technique", *Journal of Physics G: Nuclear and Particle Physics* **28** (2002) 2693, doi:10.1088/0954-3899/28/10/313.

[23] G. Cowan, K. Cranmer, E. Gross, and O. Vitells, "Asymptotic formulae for likelihood-based tests of new physics", *Eur. Phys. J. C* **71** (2011) 1554, doi:10.1140/epjc/s10052-011-1554-0, 10.1140/epjc/s10052-013-2501-z, arXiv:1007.1727. [Erratum: doi:10.1140/epjc/s10052-013-2501-z].

[24] CMS Collaboration, "Precise determination of the mass of the Higgs boson and tests of compatibility of its couplings with the standard model predictions using proton collisions at 7 and 8 TeV", *Eur. Phys. J. C* **75** (2015) 212, doi:10.1140/epjc/s10052-015-3351-7, arXiv:1412.8662.